J. Fluid Mech. (1986), vol. 167, pp. 181–198
Printed in Great Britain

Viscous fluid motion in a spinning and nutating cylinder

By THORWALD HERBERT

Department of Engineering Science and Mechanics, Virginia Polytechnic Institute and State University, Blacksburg, VA 24061, USA

(Received 26 July 1985 and in revised form 4 December 1985)

Spin-stabilized projectiles with liquid payloads can experience a severe flight instability characterized by a rapid yaw-angle growth and a simultaneous loss in spin rate. Laboratory experiments and field tests have shown that this instability originates from the internal fluid motion in the range of high viscosity. After evaluation of the experimental data and analysis of the equations for the fluid motion in a spinning and nutating cylinder, we have developed a simple model of this flow. Disregarding the finite length of the cylinder, this model provides the flow field and the viscous contribution to the liquid moments in analytical form. At low Reynolds number, the flow field agrees well with computational results for the centre section of a cylinder of aspect ratio 4.3. The roll moment caused by this flow largely agrees with experimental data for a wide range of Reynolds numbers. Estimates of the temperature variation indicate that discrepancies at very low Reynolds numbers may originate from associated changes of the viscosity during the experiments.

1. Introduction

It is well known that spin-stabilized shells carrying liquid payloads can suffer dynamical instability. For cylindrical cavities and low viscosity of the liquid, the instability due to basically inviscid inertial waves can be predicted by the Stewartson–Wedemeyer theory (Stewartson 1959; Wedemeyer 1966). This theory rests on the boundary-layer approach and is, therefore, restricted to the range of sufficiently large Reynolds numbers. The instability of certain shells like the XM761 (D'Amico 1977; 1978), however, escapes such a prediction and is also distinguished in character owing to the rapid loss in spin rate. Experiments with a full-scale liquid-filled cylinder (Miller 1982) and subsequent field tests (D'Amico & Miller 1979) establish that this new flight instability is most pronounced for liquid fills of very high viscosity.

We conduct a theoretical analysis of this problem in order to support the ongoing experiments and to independently obtain insight into the anatomy of the flow phenomena. The initial steps of this analysis are reported elsewhere (Herbert 1982): evaluation of the experimental database, dimensional analysis, scaling aspects, governing equations, and discussion of various simplifying assumptions. Two observations in this earlier work led to the approach discussed in the following. First, if the despin (negative roll) moments (Miller 1982) and void observations (Miller 1981) are correlated with the Reynolds number Re, at least three regions can be distinguished. At low Re, the despin moment increases proportional to Re, and the void in a partially filled cylinder is parallel to the spin axis. This suggests a simple fluid motion that is essentially independent of the axial coordinate, except in the neighbourhood of the end walls. In a middle range of Re, the despin moment assumes

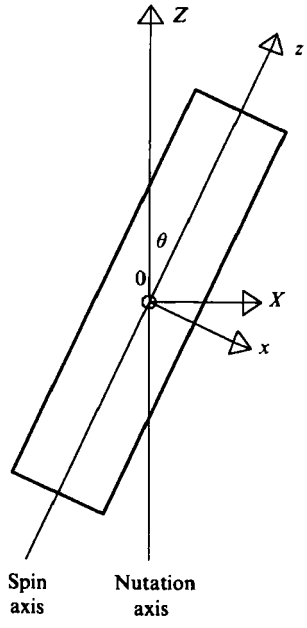

FIGURE 1. Definition sketch.

a maximum, and a wavy distortion of the void seems to indicate a cellular structure of the fluid motion. This cellular motion can, in principle, originate from hydrodynamic instability of the basic flow with respect to axially periodic disturbances. At still higher Reynolds numbers, the despin moment decreases with increasing Re in a manner not clearly defined by the few available data points. The void observations indicate, however, that the motion ultimately becomes turbulent.

The second observation is the appearance of the nutation rate and angle as a small parameter in the equations for the deviation from solid-body rotation. The forcing term due to nutation can be considered small enough for linearization of the equations in the situations of practical interest.

In the following, we describe the development of a simple system of equations for the basic flow. Analytical solutions are given for the flow field, for the liquid moments, and for the rate of change of temperature. A comparison is made with computer simulations of the flow (Vaughn, Oberkampf & Wolfe 1983; 1985) and with experimental data for the moments (Miller 1982).

2. Governing equations

We consider the motion of a fluid of density ρ and viscosity μ in a cylinder of radius a and length $2c$ that rotates with the spin rate ω about its axis of symmetry, the z-axis. We consider the motion with respect to the nutating coordinate system x, y, z. This system is obtained from the inertial system X, Y, Z, by a rotation with the nutation angle θ about the axis $Y = y$. Therefore, x is in the (Z, z)-plane, and this plane rotates about the Z-axis with the nutation rate Ω. The two axes of rotation intersect in the centre of mass of the cylinder, as shown in figure 1. We consider $\omega > 0$, Ω, and $0 \leqslant \theta \leqslant \frac{1}{2}\pi$ as constant. This is in some contrast to the experimental procedures for measuring the despin moment (Miller 1982). In these experiments, the apparatus is

held at constant conditions until a steady (or quasi-steady) flow is established. After shut-down of the spin drive, the decrease of ω as a function of time is recorded in order to obtain the roll moment.

The fluid motion is governed by the Navier–Stokes equations written in the nutating coordinate system:

$$\rho\left[\frac{D\boldsymbol{V}_{\mathrm{n}}}{Dt}+2\boldsymbol{\Omega}\times\boldsymbol{V}_{\mathrm{n}}+\boldsymbol{\Omega}\times(\boldsymbol{\Omega}\times\boldsymbol{r})\right]=-\nabla P_{\mathrm{n}}+\mu\nabla^2\boldsymbol{V}_{\mathrm{n}}, \tag{1a}$$

$$\nabla\cdot\boldsymbol{V}_{\mathrm{n}}=0. \tag{1b}$$

$\boldsymbol{V}_{\mathrm{n}}$ is the velocity measured in the nutating frame, P_{n} the pressure, and $\boldsymbol{r}$ the position vector. The body force due to gravity has been disregarded. Equations (1) are subject to the no-slip and no-penetration conditions at the cylinder walls.

It is convenient (Herbert 1982) to split the velocity and pressure fields according to

$$\boldsymbol{V}_{\mathrm{n}}=\boldsymbol{V}_{\mathrm{s}}+\boldsymbol{V}_{\mathrm{d}},\quad P_{\mathrm{n}}=P_{\mathrm{s}}+P_{\mathrm{d}}, \tag{2}$$

where $\boldsymbol{V}_{\mathrm{s}}$, P_{s} describe the state of pure solid-body rotation, whereas $\boldsymbol{V}_{\mathrm{d}}$, P_{d} represent the deviation from solid-body rotation. The advantage of this isolated view on the deviation is obvious: $\boldsymbol{V}_{\mathrm{d}}$ and the reduced pressure P_{d} are responsible for the observed flight instability. A glance at the equations shows that $\boldsymbol{V}_{\mathrm{d}}\equiv 0$ and $P_{\mathrm{d}}\equiv 0$ if either one of the following conditions is satisfied: $\omega=0$, $\Omega=0$, $\theta=0$ or $\mu\to\infty$ (solid fill).

The equations for $\boldsymbol{V}_{\mathrm{d}}$, P_{d} are written in terms of non-dimensional quantities $\boldsymbol{v}_{\mathrm{d}}$, p_{d}. We use a, ω, and ρ for scaling length, time and mass. Note that this choice is ambiguous (Herbert 1982) and excludes the case $\omega=0$ which lacks practical interest. The problem then depends on four non-dimensional parameters:

$$\lambda=\frac{c}{a}\quad\text{aspect ratio,}$$

$$\theta\quad\text{nutation angle,}$$

$$\tau=\frac{\Omega}{\omega}\quad\text{frequency,}$$

$$Re=\frac{\rho\omega a^2}{\mu}\quad\text{Reynolds number.}$$

The aspect ratio enters the solution only through the boundary conditions. The boundary conditions on $\boldsymbol{v}_{\mathrm{d}}$ are homogeneous.

In cylindrical coordinates r, ϕ, z, the equations for the non-dimensional deviation velocity $\boldsymbol{v}_{\mathrm{d}}=(v_r, v_\phi, v_z)$ and pressure p_{d} take the form

$$\frac{1}{r}\frac{\partial}{\partial r}(rv_r)+\frac{1}{r}\frac{\partial v_\phi}{\partial\phi}+\frac{\partial v_z}{\partial z}=0, \tag{3a}$$

$$\mathrm{D}'v_r-\frac{v_\phi^2}{r}-2(1+\tau_z)v_\phi+2\tau_\phi v_z=-\frac{\partial p_d}{\partial r}+\frac{1}{Re}\left[\mathrm{D}''v_r-\frac{v_r}{r^2}-\frac{2}{r^2}\frac{\partial v_\phi}{\partial\phi}\right], \tag{3b}$$

$$\mathrm{D}'v_\phi+\frac{v_r v_\phi}{r}+2(1+\tau_z)v_r-2\tau_r v_z=-\frac{1}{r}\frac{\partial p_d}{\partial\phi}+\frac{1}{Re}\left[\mathrm{D}''v_\phi-\frac{v_\phi}{r^2}+\frac{2}{r^2}\frac{\partial v_r}{\partial\phi}\right], \tag{3c}$$

$$\mathrm{D}'v_z+2\tau_r v_\phi-2\tau_\phi v_r=-\frac{\partial p_d}{\partial z}-2r\tau_r+\frac{1}{Re}\mathrm{D}''v_z, \tag{3d}$$

where

$$\mathrm{D}' = \frac{\partial}{\partial t} + \frac{\partial}{\partial \phi} + v_r \frac{\partial}{\partial r} + \frac{v_\phi}{r} \frac{\partial}{\partial \phi} + v_z \frac{\partial}{\partial z},$$

$$\mathrm{D}'' = \frac{\partial^2}{\partial r^2} + \frac{1}{r} \frac{\partial}{\partial r} + \frac{1}{r^2} \frac{\partial^2}{\partial \phi^2} + \frac{\partial^2}{\partial z^2},$$

and

$$\tau_r = -\epsilon \cos\phi, \quad \tau_\phi = \epsilon \sin\phi, \quad \tau_z = \tau \cos\theta, \quad \epsilon = \tau \sin\theta. \tag{4}$$

The primary effect of nutation is contained in the ϕ-periodic force term $-2r\tau_r = 2\epsilon r \cos\phi$ in the z-momentum equation (3d). If this term vanishes throughout, $\epsilon = 0$, equations (3) support a trivial solution $\boldsymbol{v}_\mathrm{d} \equiv 0$, $p_\mathrm{d} \equiv 0$.

The system (3) of equations is similar to the system numerically solved by Vaughn *et al.* (1983; 1985), but simplified by introducing the reduced pressure p_d. We also note that this system supports certain symmetries. Let v_r, v_ϕ, v_z and p_d be the solution at point r, ϕ, z, then the velocities and pressure at the corresponding point $r, \phi+\pi, -z$ are v_r, v_ϕ, $-v_z$ and p_d. These symmetries can be exploited for essential savings in computational work.

2.1. *Linearized equations*

For sufficiently small $\epsilon \neq 0$, it is obvious that the deviation velocity is of order $O(\epsilon)$. In the situations of practical interest, $\epsilon = (\Omega/\omega)\sin\theta$ turns out to be a rather small parameter. Even a conservative estimate with $\Omega \leqslant 500$ r.p.m., $\omega \geqslant 3000$ r.p.m., and $\theta \leqslant 20°$ provides values of $\epsilon \leqslant 0.057$. Consequently, it seems well justified to linearize the equations in ϵ. This linearization imposes no restriction on the Reynolds number.

While the continuity equation remains unaffected, linearization of the momentum equations provides

$$\mathrm{D}^* v_r - 2(1+\tau_z) v_\phi = -\frac{\partial p_\mathrm{d}}{\partial r} + \frac{1}{Re}\left[\mathrm{D}'' v_r - \frac{v_r}{r^2} - \frac{2}{r^2}\frac{\partial v_\phi}{\partial \phi}\right], \tag{5a}$$

$$\mathrm{D}^* v_\phi + 2(1+\tau_z) v_r = -\frac{1}{r}\frac{\partial p_\mathrm{d}}{\partial \phi} + \frac{1}{Re}\left[\mathrm{D}'' v_\phi - \frac{v_\phi}{r^2} + \frac{2}{r^2}\frac{\partial v_r}{\partial \phi}\right], \tag{5b}$$

$$\mathrm{D}^* v_z = -\frac{\partial p_\mathrm{d}}{\partial z} - 2r\tau_r + \frac{1}{Re}\mathrm{D}'' v_z. \tag{5c}$$

where

$$\mathrm{D}^* = \frac{\partial}{\partial t} + \frac{\partial}{\partial \phi}.$$

The system (3a), (5a)–(5c) of equations is still quite difficult to solve. Any serious attempt to satisfy all boundary conditions leads directly to a purely computational approach. Use of the boundary-layer approximation would simplify the task but seems inappropriate in the interesting range of low Reynolds numbers.

3. The core flow

We recall that the flow in a relatively long cylinder (aspect ratio $\lambda = 4.3$) at low Reynolds number is expected to have a rather simple structure and to provide a roll moment proportional to Re (Herbert 1982). Closer analysis of the equations suggests that this flow exhibits little axial variation over much of the cylinder length. The effect of the end walls will be essential only over an axial distance of $O(1)$ from the

ends. Therefore, we have relaxed the boundary conditions at the end walls. In this way, we seek a steady flow in a finite segment of an infinitely long cylinder.

The z-independent force term in (5c) can be balanced only by a purely axial deviation velocity. It is consistent with the linearized equations to assume a solution in the form

$$v_d = (0, 0, v_z), \quad p_d = 0. \tag{6}$$

Moreover, since v_z is of order $O(\epsilon)$ and periodic in ϕ, we write

$$v_z = v_z(r, \phi) = 2\epsilon\,[f(r)\cos\phi + g(r)\sin\phi], \tag{7}$$

where f and g are the imaginary and real parts, respectively, of the complex function

$$F(r) = g(r) + \mathrm{i}f(r). \tag{8}$$

Substituting (6)–(8) into the linearized equations and the no-slip conditions at the cylinder wall provides

$$r^2F'' + rF' - (1 + \mathrm{i}\,Re\,r^2)\,F = -\mathrm{i}\,Re\,r^3, \tag{9a}$$

$$F = 0 \quad \text{at} \quad r = 1, \tag{9b}$$

$$F \text{ finite at } r = 0, \tag{9c}$$

where (9c) is necessary for a physical solution. The primes denote d/dr.

3.1. *Solution for $Re \to 0$ and $Re \to \infty$*

For $Re \to 0$, the solution of (9) can be found in the form of series expansions in Re,

$$f = \tfrac{1}{8}Re(r - r^3) - \tfrac{1}{9216}\,Re^3\,(7r - 12^3 + 6r^5 - r^7) + O(Re^5), \tag{10a}$$

$$g = \tfrac{1}{192}\,Re^2\,(2r - 3r^3 + r^5) + O(Re^4). \tag{10b}$$

With higher terms included, these series converge for $Re \leqslant 12$.

In the limit $Re \to \infty$, one obtains

$$f \to 0, \quad g \to r, \quad \text{as} \quad Re \to \infty. \tag{11}$$

Owing to the loss of the highest derivatives, however, this solution cannot satisfy the boundary conditions (9b) and is valid only outside thin boundary layers near the wall at $r = 1$.

Even without any knowledge of the solution in the intermediate range, the different character of the basic flow at low and high Reynolds numbers is evident. At low Re, the component f in the (x, z)-plane $\phi = 0$ dominates the solution. At high Re, f is negligible except near the wall of the cylinder while g in the (y, z)-plane $\phi = 90°$ is dominating. One might well expect that the initial linear increase of f with Re and the change in the flow structure is related to the observed properties of the roll moment.

3.2. *Solution for arbitrary values of Re*

In earlier work (Herbert 1983), we have applied a spectral collocation method for numerically solving a real system of equations for f and g equivalent to (9). Series in odd Chebyshev polynomials for the interval $0 \leqslant r \leqslant 1$ provide accurate solutions at rather low truncation. This experience together with the minor effect of harmonics in the azimuthal direction at small ϵ suggests the use of spectral methods for efficiently solving the nonlinear equations (3).

Here, we derive an analytical solution for the core flow in a sufficiently long

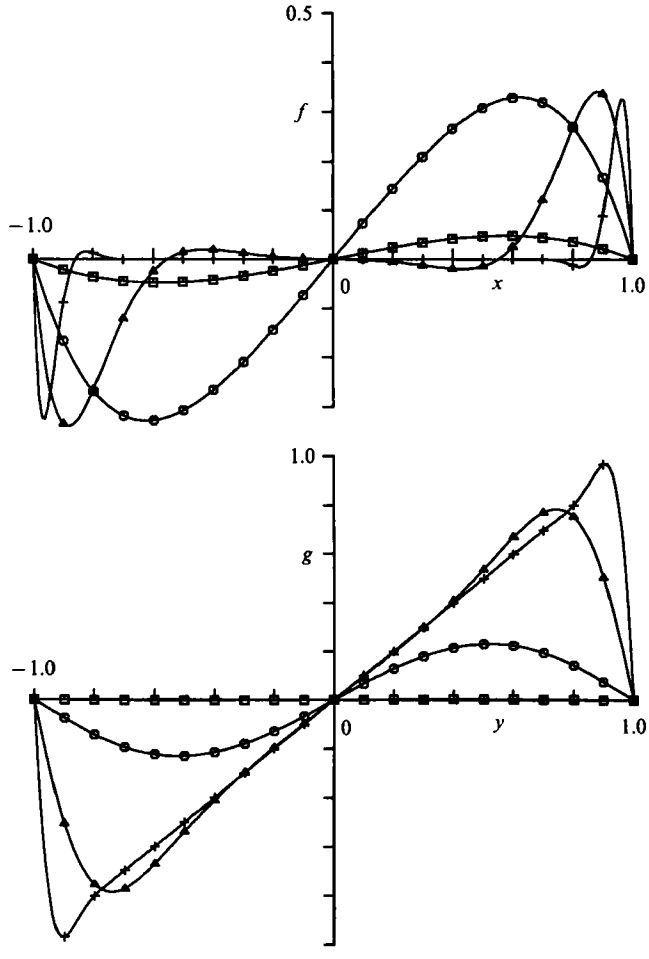

FIGURE 2. Components f and g of the axial velocity $v_z/(2\epsilon)$ for various Reynolds numbers: □, $Re = 1$; ○, 10; ▲, 10^2; +, 10^3.

cylinder. A particular solution of the inhomogeneous equation (9a) is $F_0 = r$, whereas the homogeneous part of (9a) is the equation for the modified Bessel functions $I_1(qr)$ and $K_1(qr)$ of the complex argument qr where $q = (1+\mathrm{i})\,(\frac{1}{2}Re)^{\frac{1}{2}}$. In order to satisfy (9$c$), $K_1(qr)$ cannot contribute to the solution. Finally, (9b) provides

$$F(r) = g + \mathrm{i}f = r - \frac{I_1(qr)}{I_1(q)}. \tag{12}$$

This solution is valid for arbitrary Re but may be unstable as Re exceeds some critical value. Although expressible in simple form, the resulting flow field exhibits very interesting properties.

Rewriting the solution in terms of Kelvin functions of real argument is of little advantage for the numerical evaluation. We have used a combination of ascending series and asymptotic expansions for large arguments (Abramowitz & Stegun 1972) for evaluating $F(r)$. With the solution (12) at hand, it is straightforward to derive the approximations (10) from the ascending series for I_1 (and to explain the convergence problem for larger Re). Complementary to (11), the asymptotic expansion

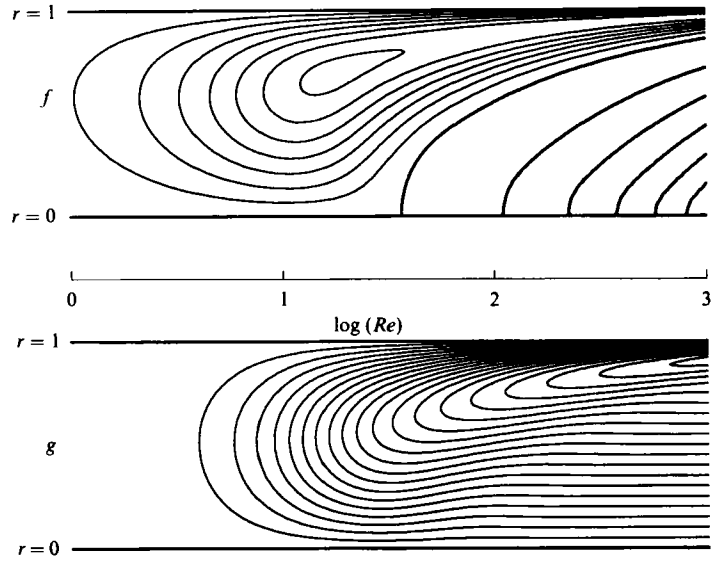

FIGURE 3. Contour lines of the components f and g of the axial velocity $v_z/(2\epsilon)$ as a function of radius r and Reynolds number Re. Intervals are 0.05; the zero level is given by the heavy line.

for large arguments, i.e. large Reynolds numbers provides the boundary-layer behaviour

$$F \approx r - r^{\frac{1}{2}}\, e^{q(r-1)}. \tag{13}$$

This expression agrees to within 1 % with (11) provided $r \leqslant 1-\delta$. The boundary-layer thickness δ can be obtained from the transcendental equation

$$\delta = (2/Re)^{\frac{1}{2}}[4.605 - \tfrac{3}{2}\ln(1-\delta)], \tag{14}$$

e.g. $\delta = 0.223$ for $Re = 1000$.

3.3. *The velocity field*

We have chosen three different graphical representations in order to illustrate the characteristic changes of the velocity distribution over the cylindrical cross-section with increasing Re. Figure 2 shows the components f (in the (x, z)-plane) and g (in the (y, z)-plane) for a wide range of Reynolds numbers. The opposite sign of the velocity at diametral points assures zero net flux of mass through the cross-section. The curves represent cuts through the contour plots of these functions of r and Re in figure 3 at the tick marks $Re = 1$, 10, 100 and 1000. Up to $Re \approx 5$, the velocity distribution is governed by f. This component never exceeds a value of 0.4, assumes a maximum at $Re \approx 20$ and retains significant size only in a shrinking neighbourhood of the wall as Re increases. The component g rapidly increases from negligible values as $Re > 5$ and approaches the linear increase with r according to (11) except near the wall at $r = 1$. In figure 4, the data of figure 2 are combined into contour plots of the axial velocity $v_z/(2\epsilon)$ over the cylindrical cross-section. These plots clearly show the shift of the velocity maximum (marked by +) from $\phi \approx 0$ at $Re = 1$ to $\phi \approx 90°$ at $Re = 1000$. Figure 4 (*d*) also illustrates the ramp-like velocity distribution over most of the cross-section and the boundary layers with $\delta = 0.223$.

Superposition of the deviation velocity $\boldsymbol{V}_d$ and the solid body rotation $\boldsymbol{V}_s$ according

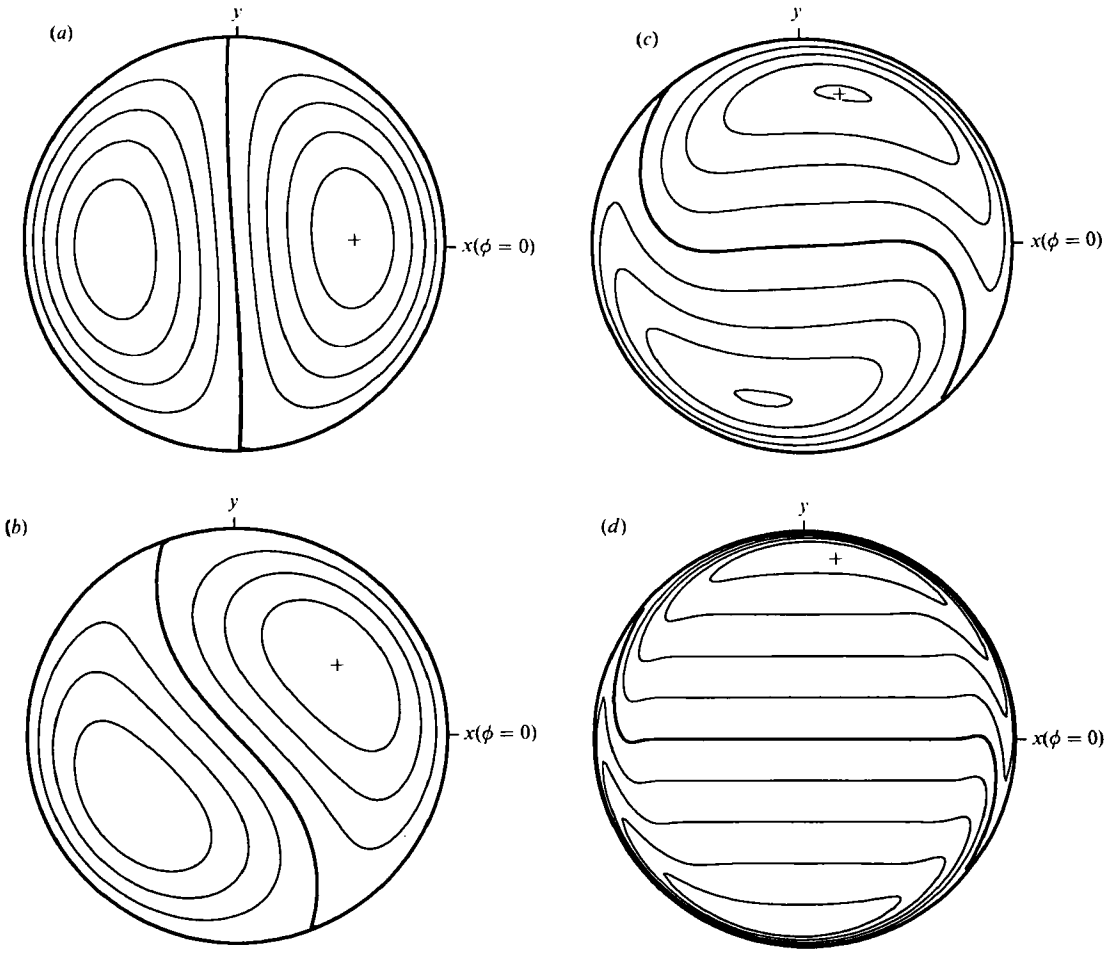

FIGURE 4. Contour lines of equal axial velocity $v_z/(2\epsilon) = \text{const.}$, for (*a*) $Re = 1$; (*b*) 10; (*c*) 10^2; (*d*) 10^3. Intervals are 0.01, 0.1, 0.2, 0.2, respectively. The zero level is given by the heavy line, the velocity maximum is marked by +.

to (2) leads to an azimuthally periodic velocity field V_n which is steady in the nutating frame. The paths of fluid elements are circular orbits about axes that are inclined to the z-axis. The inclination depends on radius and Reynolds numbers.

Figure 5 compares the dimensional velocity distributions obtained from (7), (12) with computational results for the centre cross-section ($z = 0$) of a cylinder of aspect ratio 4.3.† The agreement for $Re = 14.9$ is considered representative for the range of lower Reynolds numbers. We have repeated the numerical simulation of the flow at this Reynolds number with a modified version of the Sandia code and obtained very small components $|V_r| < 0.005$ m/s, $|V_\phi| < 0.05$ m/s at $z = 0$. These results verify our estimates and justify the use of linearized equations. Moreover, disregarding the presence of endwalls seems to have little effect in the centre portion of the cylinder. The radial distribution of V_z in the range $-3.5 \leqslant z \leqslant 3.5$ is nearly identical with the data shown in figure 5.

† The data were kindly provided by H. R. Vaughn, Sandia National Laboratories.

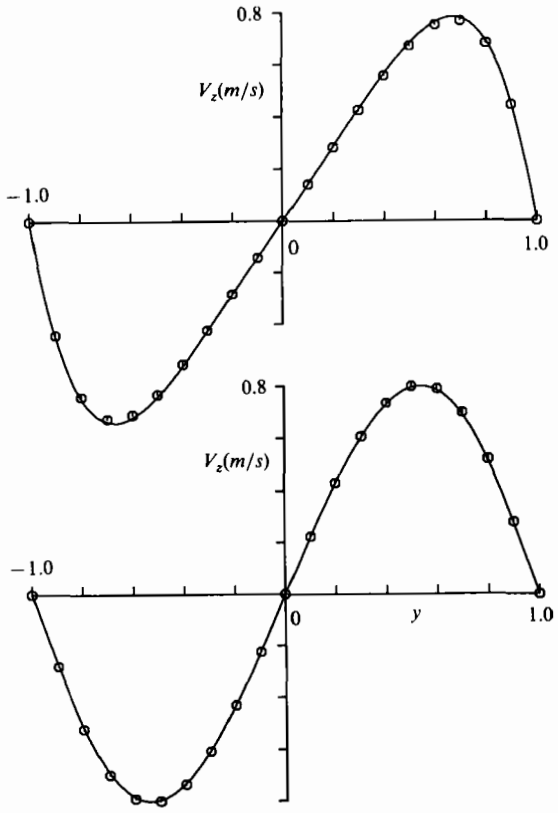

FIGURE 5. Radial distribution of the dimensional velocity V_z at $z = 0$ for $Re = 14.9$. The symbols show the numerical solution to the Navier–Stokes equations (Vaughn 1983, personal communication). Parameters: $a = 60.3$ mm, $c/a = 4.3$, $\theta = 20°$, $\omega = 3000$ r.p.m., $\Omega = 500$ r.p.m., $\rho = 1400$ kg/m^3.

Figure 6 shows a similar comparison for $Re = 45.7$. At this higher Reynolds number, we find a systematic deviation between the theoretical result and numerical results at different axial positions. We attribute this deviation to a superposed cellular motion that is not incorporated into our analysis.

4. Moments

Considering that a solid payload, or a liquid payload in pure solid-body motion, would allow for a stable flight of a projectile, we can fully concentrate on the moments caused by the deviation velocity $\boldsymbol{V}_\mathrm{d}$. With $\boldsymbol{V}_\mathrm{d} = (0, 0, \omega a v_z)$ and v_z given, the moments on a finite-length section of the cylinder can be calculated. We consider a control volume R (surface S) formed by the solid cylindrical wall and liquid surfaces at both ends. The choice of a solid wall as the cylindrical boundary is important for capturing the roll moment. Conservation of angular momentum requires

$$\boldsymbol{M} = \frac{\partial}{\partial t}\iiint_R (\boldsymbol{r}\times\boldsymbol{V}_\mathrm{d})\,\rho\,\mathrm{d}R + \iiint_R [\boldsymbol{r}\times(2\boldsymbol{\Omega}\times\boldsymbol{V}_\mathrm{d}]\,\rho\,\mathrm{d}R$$
$$+\iint_S (\boldsymbol{r}\times\boldsymbol{V}_\mathrm{d})\,(\boldsymbol{V}_\mathrm{d}\cdot\boldsymbol{n})\,\rho\,\mathrm{d}S + \iint_S (\boldsymbol{r}\times\boldsymbol{V}_\mathrm{s})\,(\boldsymbol{V}_\mathrm{d}\cdot\boldsymbol{n})\,\rho\,\mathrm{d}S. \quad (15)$$

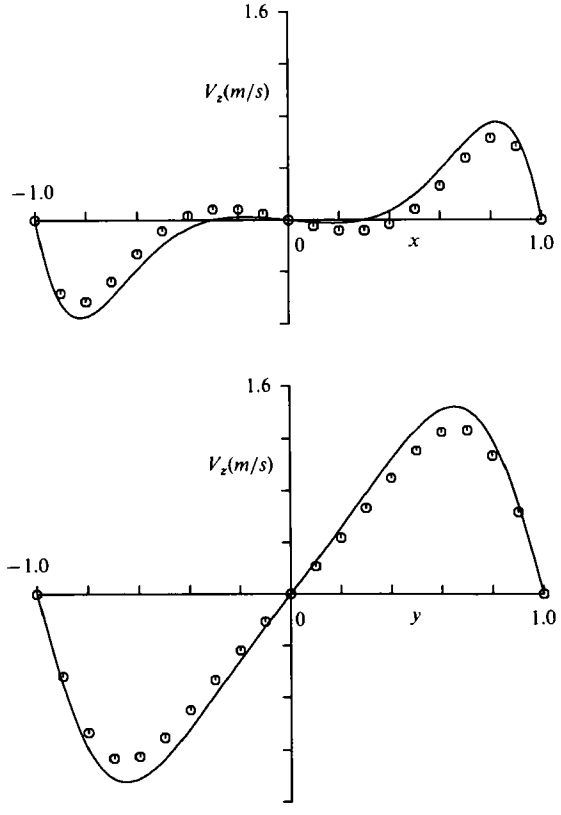

FIGURE 6. Radial distribution of the dimensional velocity V_z at $z = 0$ for $Re = 45.7$. The symbols show the numerical solution to the Navier–Stokes equations (Vaughn 1983, personal communication). Parameters: $a = 60.3$ mm, $c/a = 4.3$, $\theta = 20°$, $\omega = 3000$ r.p.m., $\Omega = 500$ r.p.m., $\rho = 1400$ kg/m^3.

where $\boldsymbol{n}$ is the outer unit normal. On the left-hand side, $\boldsymbol{M}$ is the resultant torque on the control volume. Note that the shear moment vanishes at the solid sidewall while the contributions from the liquid end surfaces cancel. On the right-hand side, the first term vanishes for steady $\boldsymbol{V}_d$. The second term originates from Coriolis forces in the nutating system. The third term vanishes since $\boldsymbol{V}_d$ has only an axial component. The last term provides the net rate of angular momentum flux through the control surface.

Substitution of $\boldsymbol{V}_d$ leads to the following expressions for the Cartesian components of $\boldsymbol{M}$:

$$M_x = m_1(2\Omega\, a \sin\theta)\,(\omega a)\, m_x,\ m_x = -\int_0^1 r^2 f\, \mathrm{d}r, \tag{16a}$$

$$M_y = m_1(2\Omega\, a \sin\theta)\,(\omega a)\, m_y,\ m_y = -\int_0^1 r^2 g\, \mathrm{d}r, \tag{16b}$$

$$M_z = m_1(2\Omega\, a \sin\theta)^2\, m_z,\ m_z = \int_0^1 r^2 f\, \mathrm{d}r = -m_x, \tag{16c}$$

where $m_1 = 2\pi\rho a^2 c$ is the liquid mass in the cylinder. In this form, the components M_x, M_y represent the net rate of angular momentum flux through the liquid ends, whereas the roll moment M_z is solely due to Coriolis forces. A close relation between roll moment M_z and yaw moment M_x has also been found by Murphy (1984, 1985). Note that M_x, M_y after division by $m_1\omega^2 a^2$ clearly are of order $O(\epsilon)$. M_z however is

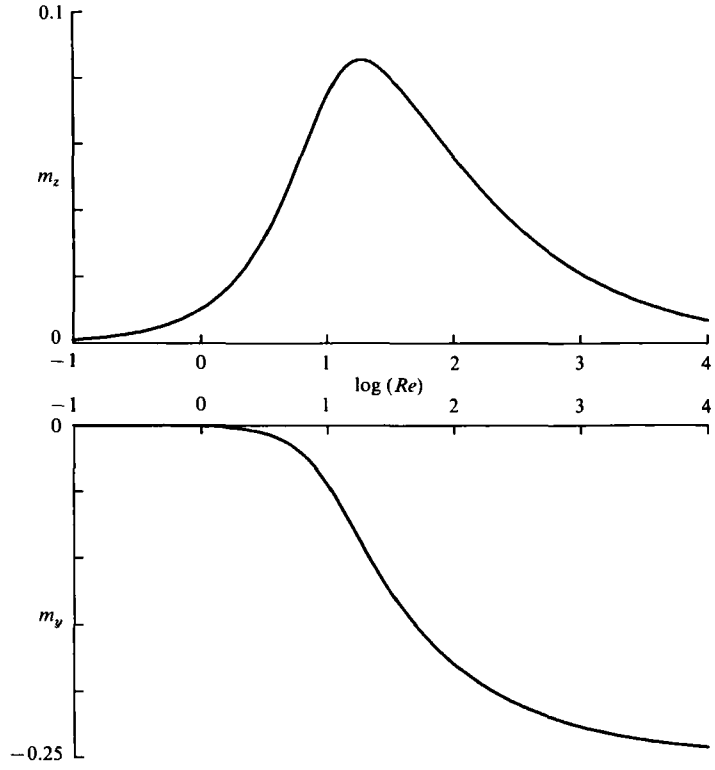

FIGURE 7. The non-dimensional coefficients m_z, m_y in (17) *vs.* the Reynolds number Re.

of order $O(\epsilon^2)$, and the question arises whether (16*c*) will be affected by second-order terms. Analysis of higher-order approximations† indicates, however, that (16*c*) is correct to within $O(\epsilon^2)$.

A different physical interpretation of the moments can be derived using the differential equation (9*a*), integrating by parts, applying (9*b*), and separating real and imaginary parts:

$$m_z = -m_x = \int_0^1 r^2 f \, \mathrm{d}r = -\frac{g'(1)}{Re}, \tag{17a}$$

$$m_y = -\int_0^1 r^2 g \, \mathrm{d}r = -\frac{f'(1)}{Re} - \frac{1}{4}. \tag{17b}$$

In this form, the moments are directly related to the shear forces at the cylindrical sidewall, $r = 1$. Since $f'(1) < 0$, $g'(1) < 0$, the roll moment M_z is always positive (even for $\Omega < 0$), while M_x is negative for $\Omega > 0$ and changes sign with Ω. For small Re, the series (10) provide the approximations

$$m_z \approx \frac{Re}{96}, \quad m_y \approx -\frac{Re^2}{1536}, \tag{18}$$

that can be used for quick estimates up to $Re \leqslant 10$. The linear increase of m_z and M_z with Re is consistent with the experimental data. From the analytical solution (10), we obtain

$$F'(1) = g'(1) + \mathrm{i} f'(1) = 2 - \frac{qI_0(q)}{I_1(q)}. \tag{19}$$

† Detailed results for higher-order approximations will be published elsewhere.

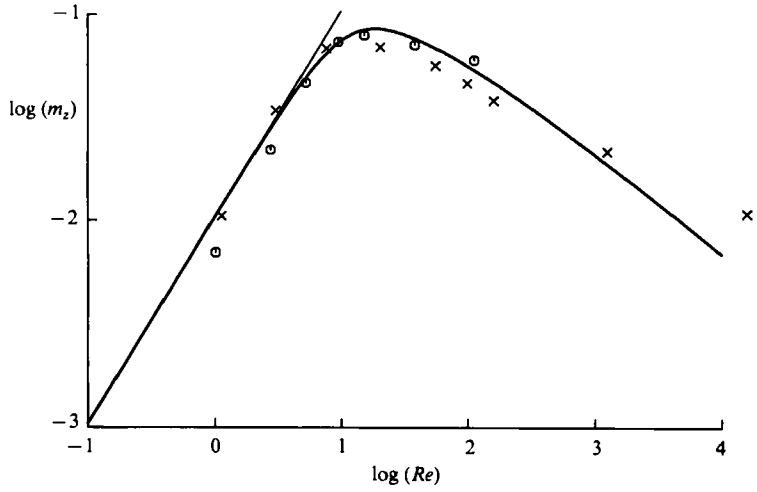

FIGURE 8. Comparison of the theoretical result for m_z with: ×, experimental data (Miller 1982); ○, computational results (Vaughn *et al.* 1985). The straight line shows the asymptotic law $m_z \approx Re/96$.

Substitution into (17) provides the variation of m_z, m_y with the Reynolds number shown in figure 7. The coefficient m_z assumes a pronounced maximum at $Re \approx 19$. The occurrence of this maximum was earlier thought to originate from hydrodynamic instability with respect to a cellular motion. Here, we find a simple explanation in the properties of the axial velocity component f in the (x, z)-plane and the derivative $g'(1)$. The coefficient m_y is negligible for $Re < 5$, sharply decreases with increasing Re and reaches an asymptotic value of $m_y \to -\frac{1}{4}$ as $Re \to \infty$. Hence, for $\Omega > 0$, M_y tends to reduce the pitch moment due to the solid body rotation. We note, however, that these moments represent only the effect of viscous shear at the cylindrical sidewall. Shear at the endwalls and the contribution of the pressure are neglected.

The data base for the yaw and pitch moments is scarce. Computations by Vaughn *et al.* (1985) indicate, however, that the pressure contributions to these moments are larger (and opposite in sign) than the viscous components. Only the viscous component can be estimated from our solution. Therefore, we concentrate in the following on a detailed comparison for the roll moment.

In figure 8 we compare the asymptotic law (18) and the theoretical result (17) with experimental data (Miller 1982) and computational results (Vaughn *et al.* 1985) for the roll coefficient m_z on a doubly logarithmic scale. The initial spin rate $\omega = 4000$ r.p.m. has been used for obtaining the non-dimensional values from the experiment. For $Re < 10$, the experimental data match the analytical result as well as the asymptotic law $m_z \approx \frac{1}{96} Re$. The deviation between theoretical and computational results is probably due to a larger axial extent of the end effects at very low Reynolds numbers. Good agreement with the computational results is obtained near the maximum of m_z. The point at $Re = 113$ is close to the Reynolds number where the numerical simulation fails to converge to a steady solution, and may not be very accurate. The experiments find the maximum roll moment at slightly lower Reynolds numbers than the theoretical value. In fact, this discrepancy will increase as lower spin rates ω are used for data reduction. In view of the agreement between theoretical and computational results, the discrepancy cannot arise from the approximations employed in our analysis. A first possible source may be the effect of unsteadiness

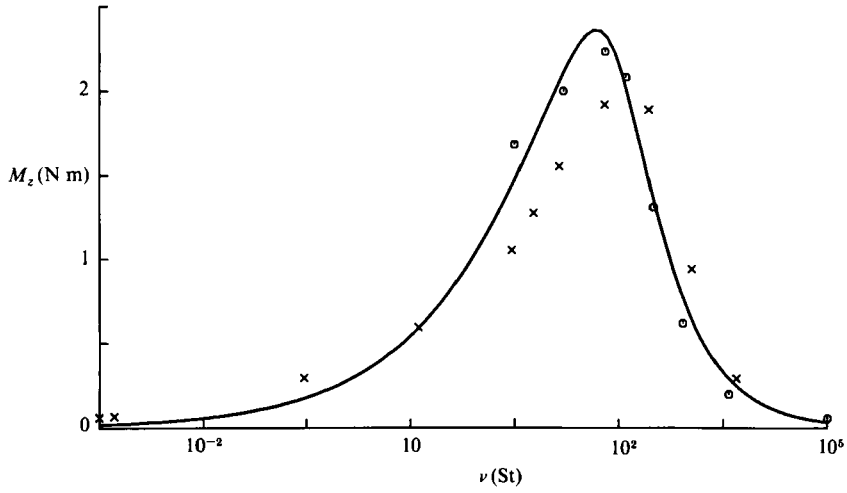

FIGURE 9. Comparison of the theoretical result for the roll moment M_z at $\omega = 3000$ r.p.m. *vs.* kinematic viscosity ν with: ×, experimental data (Miller 1982) for $\omega = 2000$–4000 r.p.m.; ○, computational results (Vaughn *et al.* 1985) for $\omega = 3000$ r.p.m. Parameters: $a = 60.3$ mm, $c/a = 4.29$, $\theta = 20°$, $\Omega = 500$ r.p.m., $\rho = 1000$ kg/m^3.

in the spin-down experiments. More likely, however, the shift is caused by changes of temperature and viscosity during the experiments. A moderate increase in temperature would reduce the viscosity of the working fluids (silicone oil, corn syrup) and hence shift the maximum to higher Reynolds numbers. Miller (personal communication) observed a temperature increase by ≈ 2.5 °C per run up to ≈ 10 °C above ambient temperature after repeated runs. Vaughn *et al.* (1985) used these values for correcting the results, with some improved agreement. We waive such a correction but discuss the temperature increase in more detail in the next chapter.

As a final observation in figure 8, we note the change in tendency for the two experimental data points at $Re > 10^3$. It is likely that the internal flow becomes unsteady and ultimately turbulent as the Reynolds number increases. Preliminary results from flow visualization in a small-scale experiment (Pierpont 1985) indicate that these two points are for a turbulent internal flow.

In figure 9 we recast experimental, computational and theoretical results for the dimensional roll moment M_z in different form. Whereas the asymptotic properties are concealed, the linear scale for M_z reveals the pronounced maximum of the roll moment for viscosities near $\nu = 10^3$ St and more clearly indicates that theory and computation yield larger maximum values than the despin experiment with the old test fixture (Miller 1982). More recent measurements with a new test fixture at higher spin rates (Miller, personal communication) provide larger maximum values slightly in excess of the theoretical result.

For the roll moment as a function of nutation angle and rate, Herbert (1983) derived from Miller's data (1982 figure 12) the empirical relation $M_z = 0.00814$ $(\Omega \sin\theta)^2$ N m. The theory provides M_z in the same form but with a somewhat larger factor of 0.0111. This comparison for a fluid of kinematic viscosity $\nu = 2.10^5$ cSt is likely to be biased by temperature effects. A notable feature of the roll moment as a function of nutation rate at different spin rates is shown in figure 10. For these parameters in the range of the maximum roll moment, the dependence of M_z on ω is non-monotonic, e.g. the data for $\omega = 9000$ r.p.m. are in between those for $\omega = 3000$

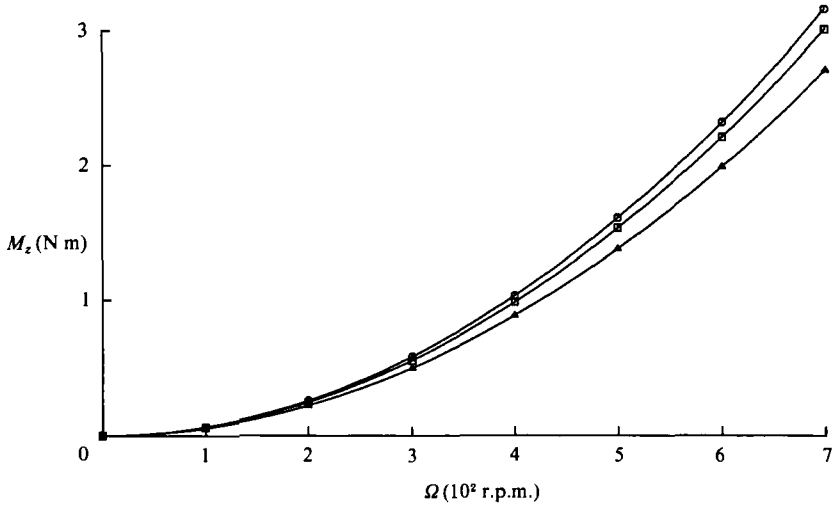

FIGURE 10. Theoretical results for the roll moment M_z *vs.* nutation rate Ω for different spin rates: ▲, $\omega = 3000$; ○, 6000; □, 9000 r.p.m. Parameters: $a = 50.4$ mm, $c/a = 4.5$, $\theta = 20°$, $\nu = 10^3$ St, $\rho = 1000$ kg/m³.

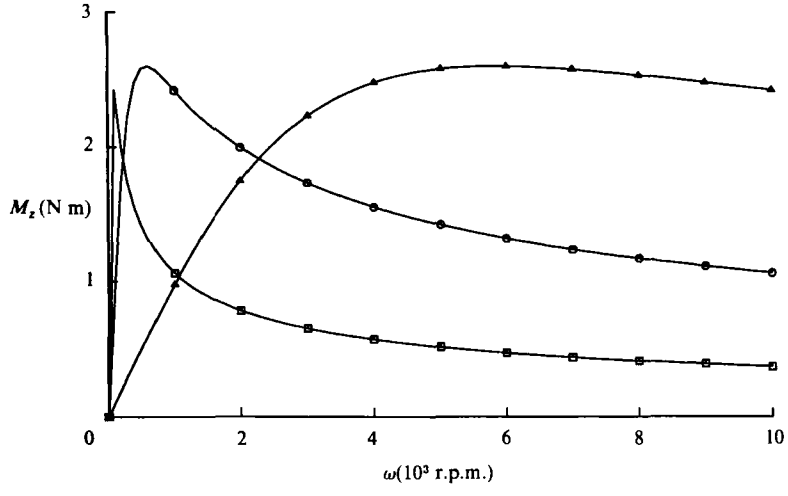

FIGURE 11. Theoretical results for the roll moment M_z *vs.* spin rate ω for different kinematic viscosities: □, $\nu = 10$, ○, 10^2, ▲, 10^3 St. Parameters: $a = 50.4$ mm, $c/a = 4.5$, $\theta = 20°$, $\Omega = 625$ r.p.m., $\rho = 1400$ kg/m³.

and 6000 r.p.m. This puzzling behaviour has been observed by Miller in experiments with the new test fixture. From the theoretical result it is obvious that M_z decreases (increases) with ω for sufficiently small (large) viscosities to the left (right) of the maximum in figure 9.

The interpretation of the experimental results has been hampered by the observation of Miller (1982) that 'the despin moment was not a function of the canister spin rate, provided a sufficient spin rate is present'. In contrast, the theoretical result (14*c*), (15*a*), (19) depends on the spin rate since $q \sim Re^{\frac{1}{2}}$ and $Re \sim \omega$ for fixed a and ν. Figure 11 shows the theoretical results for M_z as a function of the spin rate ω for viscosities $\nu = 10$, 10^2 and 10^3 St on linear scales. Note that in some range of ω, M_z

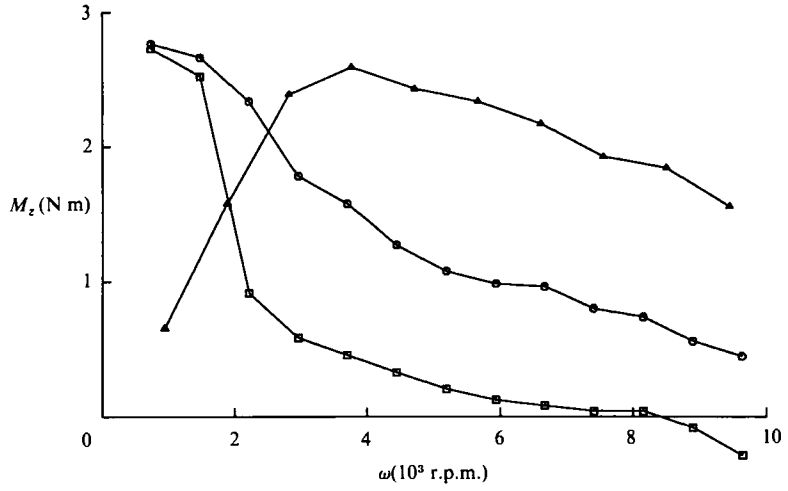

FIGURE 12. Experimental results for the roll moment M_z *vs.* spin rate ω for different kinematic viscosities: □, $\nu = 10$; ○, 10^2; ▲, 10^3 St. Parameters: $a = 50.4$ mm, $c/a = 4.5$, $\theta = 20°$, $\Omega \approx 600$ r.p.m., $\rho = 1400$ kg/m^3.

appears indeed nearly independent of the spin rate, especially for $\nu = 10^3$ St where the maximum of M_z stretches out over most of the observed range ($3000 < \omega < 9000$ r.p.m.) of spin rates. Figure 11 also shows different prototypes of behaviour that are distinguished by the position of the maximum roll moment along the ω-axis. Experimental data for similar conditions are shown in figure 12 and verify the theoretically predicted behaviour. Moreover, these data suggest major simplifications in the experimental procedures. Whereas the experimental data in figure 9 were obtained by using numerous working fluids of different viscosities, a more complete set of data can be generated by carefully monitoring the spin-down for a few runs with fluids in the range of low, medium, and high viscosities as in figure 12.

5. Temperature effect

The comparison of theoretical and computational results with experimental data seems to be biased by the effect of increasing temperature on the viscosity of the working fluid. These effects appear more pronounced at high viscosities and high spin rates. For an estimate of the rate of change of the average temperature T, we consider a control volume R (surface S) formed by liquid surfaces along the cylinder's side and end walls. The material properties are assumed to be constant and heat transfer through the surface is disregarded. Balancing the rate of change of energy with the work done on the control volume, we obtain after some simplifications

$$m_1 c_v \frac{\mathrm{d}T}{\mathrm{d}t} = \int\int_S \boldsymbol{\tau} \cdot \boldsymbol{V}_\mathrm{i} \, \mathrm{d}S, \tag{20}$$

where c_v is the specific heat, $\boldsymbol{\tau}$ the vector of tangential stresses, and $\boldsymbol{V}_\mathrm{i}$ the velocity measured in an inertial frame. Since $\boldsymbol{V}_\mathrm{d}$ is independent of z, the contributions from the cylinder ends cancel. The only contribution is due to the shear stress

$$\tau_{rz} = \mu \frac{\partial(\omega a v_z)}{\partial r}\bigg|_{r=1} = 2\mu\Omega a \sin\theta [f'(1)\cos\phi + g'(1)\sin\phi] \tag{21}$$

in the axial direction. The relevant axial component of the velocity $(\boldsymbol{\Omega} \times \boldsymbol{\omega}) \times \boldsymbol{r}$ of some point on the surface S is given by $-\Omega a \sin\theta \sin\phi$. Integration over the cylindrical surface yields

$$m_1 c_v \frac{\mathrm{d}T}{\mathrm{d}t} = -\mu(2\Omega a \sin\theta)^2 \pi a c g'(1). \tag{22}$$

After substituting for m_1 and introducing the Reynolds number, this result can be written as

$$\frac{\mathrm{d}T}{\mathrm{d}t} = \frac{\omega}{2c_v}(2\Omega a \sin\theta)^2\left(-\frac{g'(1)}{Re}\right). \tag{23}$$

Comparison with (15a) shows that the rate of change of temperature can be directly expressed in terms of the roll moment,

$$\frac{\mathrm{d}T}{\mathrm{d}t} = \frac{\omega}{2c_v}(2\Omega a \sin\theta)^2 m_z = \frac{\omega}{2m_1 c_v} M_z. \tag{24}$$

This result immediately shows that the temperature rise per run cannot be specified as a single number, nor should a uniform correction be applied to the experimental data. Moreover, the temperature changes increase with the spin rate, and consequently are quite different for the experiments with the old (Miller 1982) and the new test fixture. Using the maximum value $m_z \approx 0.0854$, we obtain for the 1982 experiments ($a = 60.3$ mm, $\omega = 4000$ r.p.m., $\Omega = 500$ r.p.m., $\theta = 20°$) with corn syrup ($c_v \approx 2350$ J/kg °C)) a temperature rise of $\mathrm{d}T/\mathrm{d}t = 0.036$ °C/s. Using silicone oil ($c_v \approx 1600$ J/kg °C)) in the new test fixture ($a = 55.4$ mm, $\omega = 10^4$ r.p.m., $\Omega = 600$ r.p.m., $\theta = 20°$) leads to a temperature increase of $\mathrm{d}T/\mathrm{d}t = 0.158$ °C/s.

A single run consists of three phases (Miller, personal communication). The spin-up period of ≈ 30 s is followed by a sudden start of the nutational motion and a period of ≈ 30 s in order to reach steady conditions. Finally, the shutdown of the spin drive is followed by a spin-down period of ≈ 15 s. The second period at nearly steady conditions and maximum spin rate appears most relevant to the modification of the viscosity. During this period, the kinematic viscosity of corn syrup changes according to $\nu = \nu_0 \exp(-0.119\Delta T)$, where ν_0 is the nominal kinematic viscosity at the beginning of the run. At the start of the third phase, the average temperature may have increased by $\Delta T \approx 1.07$ °C, while the viscosity dropped to $\nu \approx 0.88\nu_0$. Measurements by Miller indicated that the temperature in the cylinder after repeated runs stabilized at $\Delta T \approx 10$ °C above ambient temperature. At this level, the viscosity would be reduced to $\nu \approx 0.3\nu_0$. This effect would fully account for the systematic deviation between experimental and theoretical data in figure 9. In the more recent experiments at higher spin and nutation rates, the average temperature may have increased by as much as $\Delta T \approx 4.75$ °C over a period of 30 seconds. The value of 2.5 °C measured in the new fixture is well within the estimated range. The temperature effect on the kinematic viscosity of silicone oils, however, is relatively small. With $\nu = \nu_0 \exp(-0.014\Delta T)$, we obtain after 30 seconds $\nu \approx 0.94\nu_0$, and $\nu \approx 0.87\nu_0$ with $\Delta T = 10$ °C after repeated runs.

6. Concluding remarks

We have developed a simple model of the viscous fluid motion in a spinning and nutating cylinder. The disregard of the end walls has some obvious consequences: the turning flow near the ends and the associated contributions of pressure and shear

stresses to the moments cannot be obtained from this model. Nevertheless, we gather understanding as well as quantitative information. The velocity field of the core flow agrees well with computational results for low Reynolds numbers. The analytical result is an evident example for the formation of boundary layers. The core flow can be utilized as a basic flow in studies of hydrodynamic instability with respect to cellular motions. The parametric excitation of such cells by the azimuthally periodic deviation has been discussed by Herbert (1984). The core flow also represents the lowest-order approximation to the solution of the nonlinear equations (3) and can be extended by higher-order terms in ϵ.

The roll moment agrees well with measured and computed values, and can also be found at Reynolds numbers too large for successful numerical simulations. The roll moment originates from Coriolis forces. While the direct calculation of the yaw moment suffers from neglecting the pressure contribution, the yaw moment can be found from the roll moment using the relations given by Murphy (1984, 1985). The pitch moment remains an open issue. The estimates for the change in average temperature need further verification once more detailed data become available.

The simple form and scaling relations of our results provide guidance for sorting and evaluating the experimental database. The results also suggest various improvements in the experimental procedures. First, the changes in temperature and viscosity should be carefully monitored. With the effective viscosity known, a closer agreement between theory and observation is to be expected. Second, the yet neglected variation of the roll moment with the spin rate is considered relevant and in fact provides the roll moment in some range of Reynolds numbers. Instead of producing the data for figure 9 by using numerous viscosities at fixed spin rate, very similar data can be generated by varying the spin rate for a few fluids.

The open cooperation and sharing of data with Miles C. Miller (CRDC) and Harold R. Vaughn (Sandia Laboratories) are greatly appreciated. Ri-Hua Li deserves credit for his assistance in developing the analytical solution. This work is supported by the Army Research Office under Contract DAAG29-82-K-0129 and by the Army AMCCOM under Contract DAAK11-83-K-0011.

REFERENCES

ABRAMOWITZ, M. & STEGUN, I. A. 1972 *Handbook of Mathematical Functions.* Dover Publications.

D'AMICO, W. P. 1977 Field tests of the XM761: first diagnostic test. *Ballistic Research Laboratory, Mem. Rep.* no. 1325.

D'AMICO, W. P. 1978 Field tests of the XM761: second diagnostic test. *Ballistic Research Laboratory, Mem. Rep.* ARBRL-MR-02806.

D'AMICO, W. P. & MILLER, M. C. 1979 Flight instability produced by a rapidly spinning, highly viscous liquid. *J. Spacecraft Rockets*, **16**, 62–64.

HERBERT, TH. 1982 Fluid motion in a rotating and nutating cylinder – Part 1. Report prepared under the Scientific Services Program. *Rep. CRDC-CR*-84087 (1984).

HERBERT, TH. 1983 The flow of highly viscous fluid in a spinning and nutating cylinder. *Proc. of the 1983 Scientific Conference on Chemical Defense Research.* Aberdeen Proving Ground, MD.

HERBERT, TH. 1984 Highly viscous fluid flow in a spinning and nutating cylinder. *Proc. of the Second Army Conference on Applied Mathematics and Computing.* Troy, NY. *ARO Report* 85-1.

MILLER, M. C. 1981 Void characteristics of a liquid filled cylinder undergoing spinning and coning motion, *J. Spacecraft Rockets*, **18**, 286–288.

MILLER, M. C. 1982 Flight instabilities of spinning projectiles having nonrigid payloads. *J. Guidance, Control, Dynamics*, **5**, 151–157.

MURPHY, C. M. 1984 A relationship between liquid roll moment and liquid side moment. *Ballistic Research Laboratory, Mem. Rep.* ARBRL-MR-03347.

MURPHY, C. M. 1985 A relation between liquid roll moment and liquid side moment. *J. Guidance, Control, Dynamics*, **8**, 287–288.

PIERPONT, D. 1985 Design of an experiment for visualization of the flow in a spinning and nutating cylinder. *Senior Project Report*, VPI & SU.

STEWARTSON, K. 1959 On the stability of a spinning top containing liquid. *J. Fluid Mech.* **5**, (4), 577–592.

VAUGHN, H. R., OBERKAMPF, W. L. & WOLFE, W. P. 1983 Numerical solution for a spinning nutating fluid-filled cylinder. *Sandia Rep.* SAND 83-1789.

VAUGHN, H. R., OBERKAMPF, W. L. & WOLFE, W. P. 1985 Fluid motion inside a spinning nutating cylinder. *J. Fluid Mech.* **150**, 121–138.

WEDEMEYER, E. H. 1966 Viscous corrections to Stewartson's stability criterion. *Ballistic Research Laboratory*, Rep. 1325.